# Synthesis and characterization of ecofriendly materials zeolite from waste glass and aluminum scraps using the hydrothermal technique

Mouna Sayehi, Gérard Delahay, Hassib Tounsi

# Synthesis and characterization of ecofriendly materials zeolite from waste glass and aluminum scraps using the hydrothermal technique

**Mouna Sayehi[a*], Gérard Delahay[b], Hassib Tounsi[a]**

[a] Laboratoire des Matériaux Avancés, Ecole Nationale d'Ingénieurs de Sfax, Université de Sfax, Tunisia

[b] Institut Charles Gerhardt, UMR 5253 CNRS/UM2/ENSCM/UM1, Equipe ''Matériaux Avancés pour la Catalyse et la Santé" Ecole Nationale Supérieure de Chimie de Montpellier, 8 rue de l'Ecole Normale, 34296 Montpellier cedex, France

**Abstract:** In this study, we reported a simple and easy process for zeolite synthesis using waste glass and aluminum scraps. The silica source was obtained from glass of the end-of-life fluorescent tubes and aluminum source was scraps collected from aluminum workshop in the region of Sfax, Tunisia. The zeolitic materials were prepared by hydrothermal treatment at 60 °C for 6 days using 10 g of glass powder mixed with sodium aluminate solution prepared from aluminum scraps. In order to optimize the nature of the recovered zeolites, reaction time, particle size, aluminum concentration and liquid/solid ratio were monitored. T The starting materials and the prepared zeolites were characterized by X-Ray Diffraction (XRD), X-Ray Fluorescence (XRF), Fourier Transform Infrared Spectroscopy (FTIR), Scanning Electron Microscopy (SEM), and Nuclear Magnetic Resonance (NMR) of $^{27}Al$ and $^{29}Si$ nuclei. The characterization techniques demonstrated that the recovered solid after 6 days of crystallization at 60 °C using different particle sizes (ø <63 µm, ø <125 µm, ø <325 µm) was zeolite Na-LTA contaminated with small quantity of Na-P1.

**Keywords**: fluorescent tubes glass, aluminum scrap, zeolite, Na-LTA, hydrothermal synthesis.

## 1. Introduction

Zeolites are crystalline tectoaluminosilicates made up of $[SiO_4]$ $[AlO_4]^{5-}$ tetrahedra linked at their corners to form well-defined 3D framework. The orientation of $[SiO_4]^{4-}$ and $[AlO4]^{5-}$ tetrahedra generate pores and channels with molecular dimensions. The excess of negative charges produced by $Al^{3+}$ is compensated with alkali ($Na^+$, $K^+$...) or alkaline earth metal ions ($Ca^{2+}$, $Mg^{2+}$.) surrounded by water molecules located within the void space **[1–4].** The relevant physicochemical

properties (molecular sieving, high surface area, and high thermal and chemical stability) of zeolites derive from their specific structure. It is not surprising that zeolites found applications in many industries as sorbents, as molecular sieves, as ion exchangers in detergents, as fer- tilizers, or as catalysts in industrial processes **[3–6]**. Zeolites are easily synthesized under laboratory conditions by hydrothermal treatment of reactive alkali-metal aluminosilicate gels at temperatures between ambient and 200 ◦C and at autogenously pressures. The crystallization time varies from few hours to several days in order to improve the crystallinity of the zeolitic products **[1,2]**. Mostly, syntheses were car- ried out by mixing expensive chemical reagents which contain pure Si sources (e.g., colloidal silica, alkali silicates, silicon alkoxides) and pure Si sources (e.g., colloidal silica, alkali silicates, silicon alkoxides) and pure Al sources (e.g., aluminum (hydr)oxides, nitrates, alkoxides, sodium aluminate) **[7]**. Other reagents are required for the reaction such as the mineralizing agents (NaOH, KOH) and the structure directing agents (organic surfactants) **[1,2]**. Therefore, many studies focused in the use of alternative sources of Si and Al from cheaper and abundant sources. Several low-cost geological silicate and aluminosilicate **[8–18]** and low-cost industrial by-products **[19–41]** were recommended as inex- pensive starting materials for zeolite syntheses. Among industrial by-products, coal fly ashes are mainly employed in zeolite preparation because of the large quantities produced worldwide **[4,23,30,41–45]**. Moreover, porcelain wastes **[36,46]**, glass wastes **[34,35,38–40,47–57]** are rich sources of Si and Al that found application in zeolite prepara- tions. Low Si/Al ratio zeolites (LTA, FAU, Na-P1 and HS) are generally targeted in syntheses from glass wastes using appropriate synthesis conditions and techniques. Alves et al. **[50]** used industrial raw powder glass to prepare LTA, X and HS zeolites. Alkaline fusion technique fol- lowed by a hydrothermal treatment was adopted since the glass powder residue is difficult to zeolitize by hydrothermal treatment in basic media **[52]**. Terzano et al.**[51]** obtained by hydrothermal treatment of municipal glass and aluminum solid wastes at 60 ◦C for 7 days a zeotype material containing 30% of zeolite LTA when NaOH is used as mineralizing agent. Noviello et al. **[38]** recycled glass and aluminum packaging materials, in the perspective of circular economy, to synthe- tize zeolitic materials through an alkaline hydrothermal treatment. Sayehi et al. **[34,35]** prepared Na-P1 and Na-FAU zeolites from waste glass issued from fluorescent tubes and aluminum scraps by alkaline fusion technique followed by hydrothermal treatment. The valorization of cathode-ray-tube funnel glass **[53]** and LCD panel glass **[55]** into zeolites LTA, FAU and Na-P1 is also undertaken. In order to shorten crystallization time, microwave radiation was applied to the early-stage of the hydrothermal activation to initiate zeolitization process **[55–58]**. Majdinasab et al. **[55–57]** succeed to prepare zeolite HS and Na-P1 from residue called waste glass cullet using microwave radiation.

In our previous works **[34,35]**, we reported for the first time the co-valorization of powder glass (GP) derived from fluorescent tubes and aluminum scraps (AS) into Na-P1 and Na-FAU zeolites using alkaline fusion technique followed by hydrothermal treatment. In this study, we reported a simple and easy process for Na-LTA zeolite synthesis from GP and AS using hydrothermal technique at mild temperature (60 ◦C). The influence of reaction time, particle size, AS concentration and liquid/- solid ratio on the nature of obtained zeolites was monitored. The starting material and the zeotype samples were characterized by several tech- niques. The X-ray diffraction, Fourier-transform infrared spectroscopy and 27Al, 29Si magic angle spinning (MAS) nuclear magnetic resonance (NMR) were used for the structural characterization. The morphology, the particle size distribution and the textural properties were studied using scanning electron microscope, laser diffraction particle size analyzer and the adsorption–desorption of N2 gas at − 196 ◦C, respectively.

## 2. Experimental procedure

### 2.1. Starting materials

The aluminum source was scraps collected from aluminum workshop in the region of Sfax, Tunisia. The scraps are fragments resulting from the turning process of aluminum profiles. Before use, aluminum scraps (AS) were first dried and then sieved using stainless steel sieve (Ø < 1 mm) to remove small sand particles. After that, the sieved AS is washed with deionized water and finally dried at 105 ◦C for 12 h [34]. The silica source was obtained by crushing the glass of the end-of-life fluorescent tubes, collected from the special containers established by the administration of the National Engineering School of Sfax-Tunisia for the collection of hazardous waste [34]. Analytical grade NaOH pellets was purchased from Sigma Aldrich and 98%.

### *2.2 Synthesis procedure*

**Figure 1** reported a schematic presentation of the zeolitization of GP using conventional hydrothermal route as described by Terzano et al. [51].. At first, into 80 mL of 2.5 M sodium hydroxide solution we put a definite mass of AS. There is formation of $H_2$ bubbles which finished about 2 hours. After the filtration of the sodium aluminate solution, 10 g of GP were mixed into certain volumes of the solution (50, 100, 150 and 200 mL) then the slurry was stirred for 2 hours with magnetic stirrer at room temperature. After stirring, the slurry was kept in closed polyethylene bottles and let then to react without stirring at 60 °C at different periods. The effects of different parameters on the nature of the obtained zeolitic products were studied such as the particle sizes (< 63 μm: GP-63, <125 μm: GP-125 and <315 μm: GP -315) of the GP, the mass of aluminum scrap dissolved in the aluminate solution (0.125; 0.25; 0.5; 0.75; 1.0 g), the crystallization time (2, 4, 6, 8

days) and the ratio liquid /solid, **L/S** (5, 10, 15 and 20). The resulting products were filtered, washed with deionized water until pH below 9 and dried at 80°C for 24 h. The synthesized products are named **ZH-s-t** with ***s*** referred to the particle size of the GP (63 μm; 125 μm; 315 μm) and ***t*** to the duration of the experiment (2, 4, 6, 8 days).

### *2.3 Characterization techniques*

GP, AS and zeolitic products were characterized by different techniques. X-ray fluorescence (XRF) was used to assess chemical composition of the GP using Philips X'UNIQUE II apparatus. The chemical composition of the AS was analyzed by Thermo Scientific Niton XL3t GOLDD XRF Analyzer s for metal and alloy identification. Structural phase analysis by X-ray diffraction (XRD) was performed on a D8 AXS (DRX-Bruker D8) diffractometer, using CuKα radiation (λ = 1.540598 Å ) in which the Bragg angle (2θ) was scanned from 5° and 60°. FTIR spectra of the samples were recorded in air at RT using attenuated total reflectance Fourier transform infrared spectroscopy (ATR-FTIR). The spectra were recorded using a Perkin Elmer Fourier transform infrared spectrometer in the wave-number range 4000-400 $cm^{-1}$. The examination of the morphology of both raw materials and zeolitic products was investigated by scanning electron microscopy (SEM) with a JEOL JSM-5400 instrument. Adsorption-desorption isotherms were measured at -196 °C on a TriStar 3000 V6.04 A apparatus with $N_2$ as probe molecule. Prior to measurement the samples were degassed for 12 hours at 200 °C before adsorption. $^{27}Al$ and $^{29}Si$ MAS-NMR spectra were recorded on a Brucker 300 MHz (AMX 300) at 78.20 and 58.48 MHz, respectively. The chemical shift in ppm was obtained with respect to $AlCl_3.6H_2O$ and TMS as external references for Al and Si, respectively. Particle size distribution (PSD) of the samples was determined by laser diffraction particle size analyzer type Malvern Instruments Ltd (Mastersizer). The standard volume percentiles at 10, 50, and 90, denoted as D10, D50 and D90, respectively, were recorded from the analysis and used to calculate the width of the distribution span (S).

$$Span = \frac{D_{90} - D_{10}}{D_{50}}$$

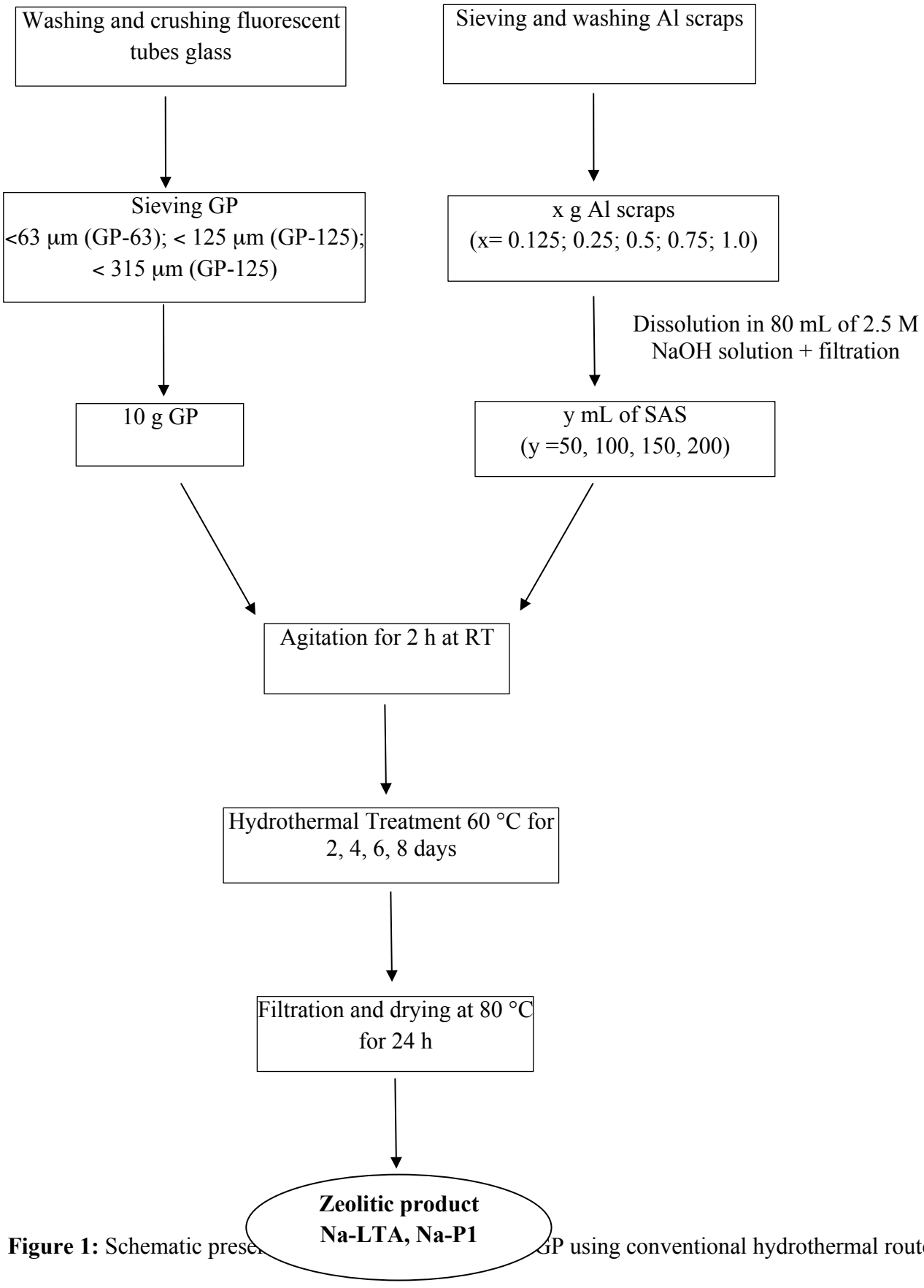


**Figure 1:** Schematic prese GP using conventional hydrothermal route.

## 3. Results and discussion

### *3.1. Characterization of the GP and AS*

The chemical composition of AS analyzed by XRF is Al-99.77 % with very small quantities of iron Fe-0.207 % and copper Cu-0.08 %. The chemical composition of GP-125 is illustrated in **Table** 1. The major oxides are $SiO_2$ (64.6 %), $Na_2O$ (21.50 %) and CaO (6.91 %). The quantities of MgO and $Al_2O_3$ are about 3.00 % and 2.59 %, respectively. The other oxides such as $K_2O$, $Fe_2O_3$, $TiO_2$, $SO_3$ and $P_2O_5$ exceed slightly the amount of 1.0 %. The chemical composition of the GP is of the soda-lime-silica type glass. The molar $SiO_2/Al_2O_3$ ratio of the GP is about 42.4; thus an additional aluminum quantity was needed to adjust the molar ratio in order to obtain low Si/Al zeolites (LTA, P, FAU and HS).

**Table 1**: Chemical composition of major and trace elements of GP-125.

| | |
|---|---|
| **$SiO_2$ (wt.%)** | 64.60 ± 0.3 |
| **$Na_2O$** | 21.50 ± 0.2 |
| **CaO** | 6.91 ± 0.09 |
| **MgO** | 3.00 ± 0.04 |
| **$Al_2O_3$** | 2.59 ± 0.06 |
| **$K_2O$** | 0.83 ± 0.03 |
| **$Fe_2O_3$** | 0.21 ± 0.01 |
| **$SO_3$** | 0.12 ± 0.01 |
| **$TiO_2$ (ppm)** | 635 ± 7 |
| **$P_2O_5$** | 556 ± 5 |
| **$ZrO_2$** | 297 ± 1 |
| **PbO** | 216 ± 1 |
| **SrO** | 165 ± 1 |
| **CuO** | 155 ± 1 |
| **$Cr_2O_3$** | 103 ± 2 |
| **$Rb_2O$** | 65 ± 1 |

**Figure 2** reported the X-ray diffraction profile of **GP-125**. The broad hump between 15 °and 35° 2θ indicated the presence of an amorphous phase. The SEM micrograph of the GP-125 is presented in **figure 3.** Glass fragments with irregular shape and angular edges are observed in **figure 3A**. This morphology is due to the grinding of the glass waste. At high magnification **(figure 3B)**, we also observe needle shaped particles. On the other hand, **GP-125** has wide particle distribution which is

ranged approximately between 1-100 µm. The particle size distribution (PSD) determined by laser diffraction confirmed the MEB results in which the sample presented bimodal distribution (**figure 4)**. The first population is located in the range of 0.3–10 µm with mode M1= 4 µm and represents 10%. The second one which represents 90% had particle size in the range of 10–120 µm with mode M2 = 100 µm. The granulometric parameters of the sample are inserted in **figure 4.** The median particle diameter D50 is about 78 µm. The span value S = 2.7; which measures the spread of the particle size distribution; shows that **GP-125** sample has a significant size difference between the particles.

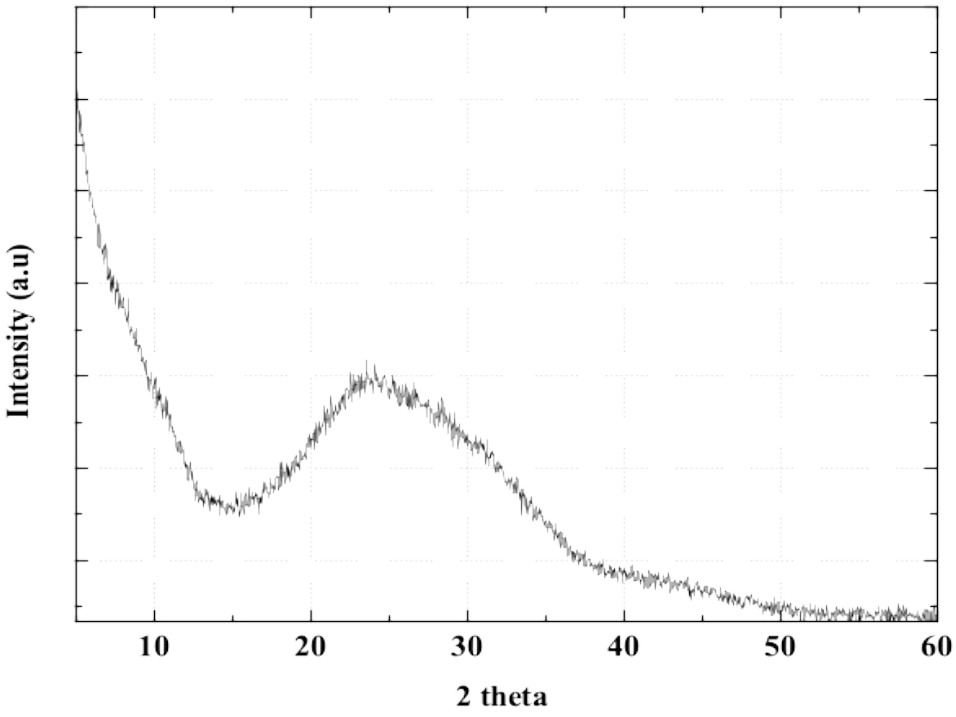


**Figure 2:** XRD pattern of GP-125.

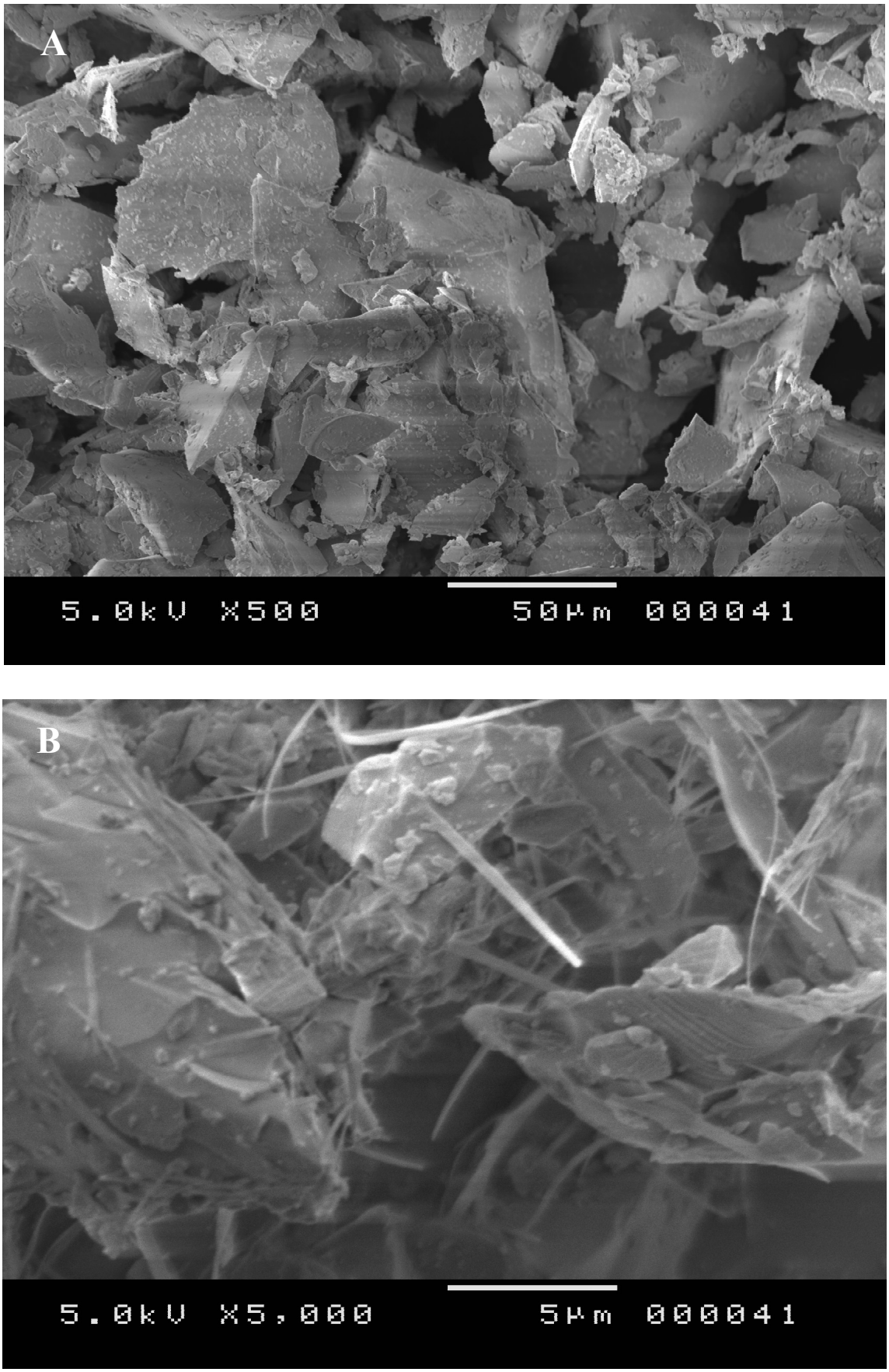


**Figure 3:** SEM photomicrographs of GP-125 at different magnifications **(A)** × 500, **(B)** ×5000.

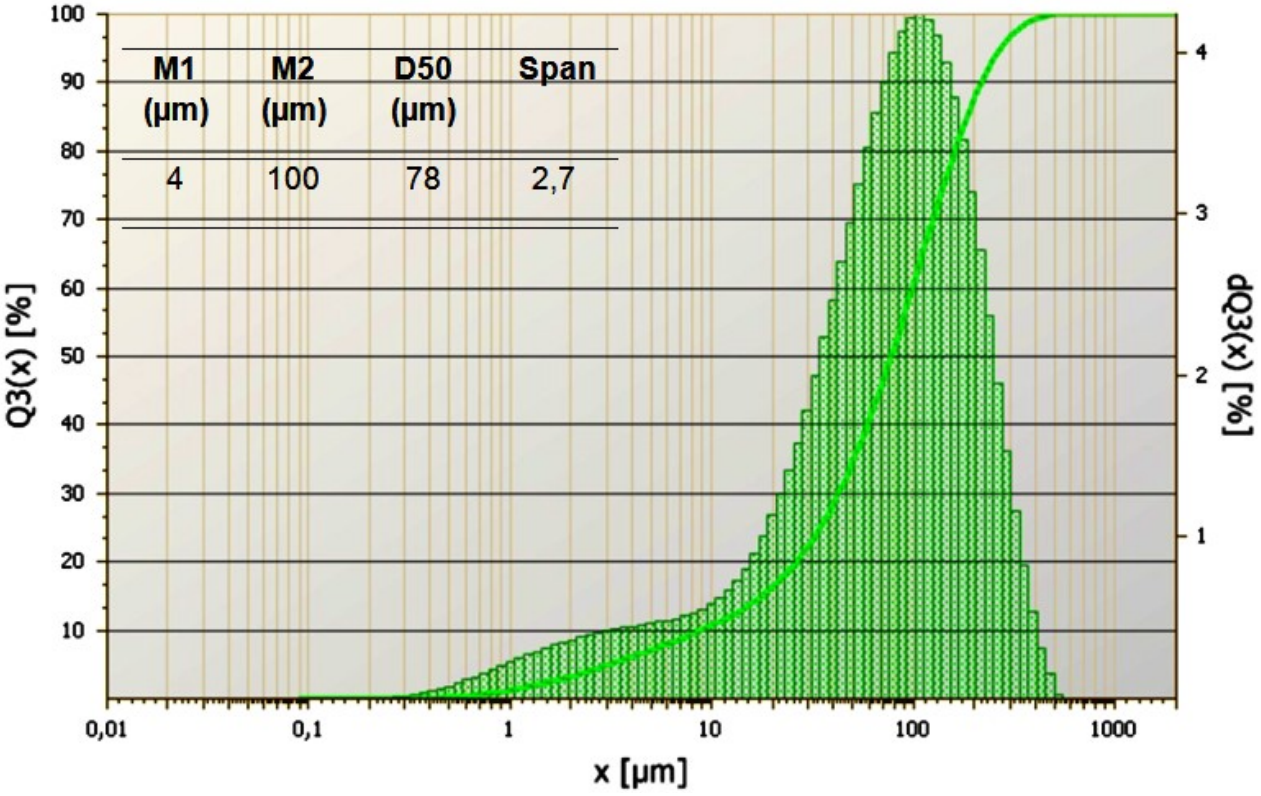


**Figure 4:** PSD using laser diffraction particle size analyzer of GP-125.

The FTIR transmittance spectrum of GP-125 is reported in **figure 5**. The feature appearance of the spectrum is characteristic of that of a soda-lime silica glass **[47, 58-61]**. Thus, the main intense band around 1040 $cm^{-1}$ with two shoulders at 1200 and 930 $cm^{-1}$ is attributed to asymmetric stretching modes of the amorphous Si-O-Si network. The less intense signal at 770 $cm^{-1}$ is originating from symmetric Si-O-Si stretching. It is worth mentioning that the band at 1040 $cm^{-1}$ correspond to the asymmetric stretching vibrations of $Q^3$ entities and the shoulders at 1200 and 930 $cm^{-1}$ to $Q^4$ and $Q^2$ entities, respectively **[61-63]**. The symbol Q represents one $SiO_4^{4-}$ tetrahedron and a superscript denotes the number of bridging oxygen atoms. The peaks at 471 $cm^{-1}$ can be attributed to bending modes of Si–O–Si or O–Si–O. The presence of carbonate was confirmed by the bands at 1430 and 1410 $cm^{-1}$. The bands at 3785 and 3665 $cm^{-1}$ are attributed to different stretching modes of silanol Si(OH) groups. Those at 3500 and 1600 $cm^{-1}$ are assigned to O-H stretching and bending modes in water group, respectively. Bands around 2929 and 2850 $cm^{-1}$, are attributed to asymmetric and symmetric stretching modes of interstitial $H_2O$ molecules, respectively.

FTIR results were confirmed by the $^{29}Si$ MAS-NMR technique **(figure 6)**. $^{29}Si$ MAS-NMR spectrum shows an intense and broad (Full Width at Half Maximum, FWHM= 20 ppm) asymmetric

signal at −92 ppm laying between -70 and -120 ppm which is consistent with a range of amorphous $^{1}Q$–$^{4}Q$ silicate units [61]. So, the main peak at -92 ppm is relative to predominant $^{3}Q$ species, the shoulder at -103 ppm is attributed to $^{4}Q$ species and the small peak at around -80 ppm to $^{2}Q$ species. On the other hand, $^{27}Al$ MAS-NMR spectrum of GP-125 reported in **figure 7** exhibits intense and broad peak at 54 ppm (FWHM= 25 ppm). This peak is typical of highly disorganized tetrahedral aluminum species within the amorphous glass system.

According to the chemical shift ranges of silicon noted on the $^{29}Si$-NMR spectrum and the large amount of alkalis ($Na_2O + K_2O = 22.33\%$) in the **GP-125**, we can assume that the majority of species are $Q^3$ and eventually $Q^3(1Al)$ species given the low amount of aluminum.

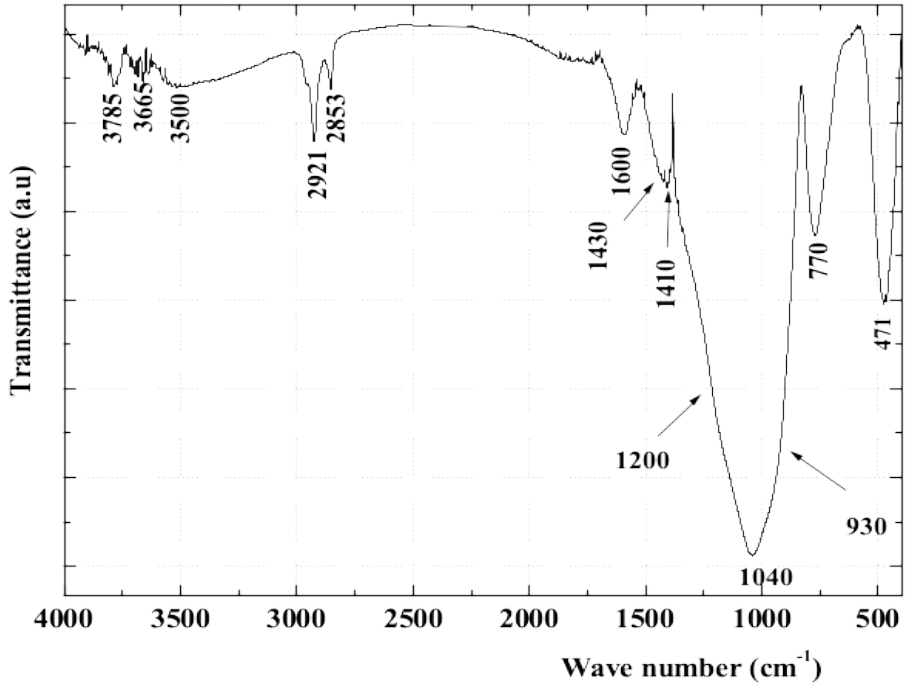


**Figure 5.** Infrared spectrum of GP-125.

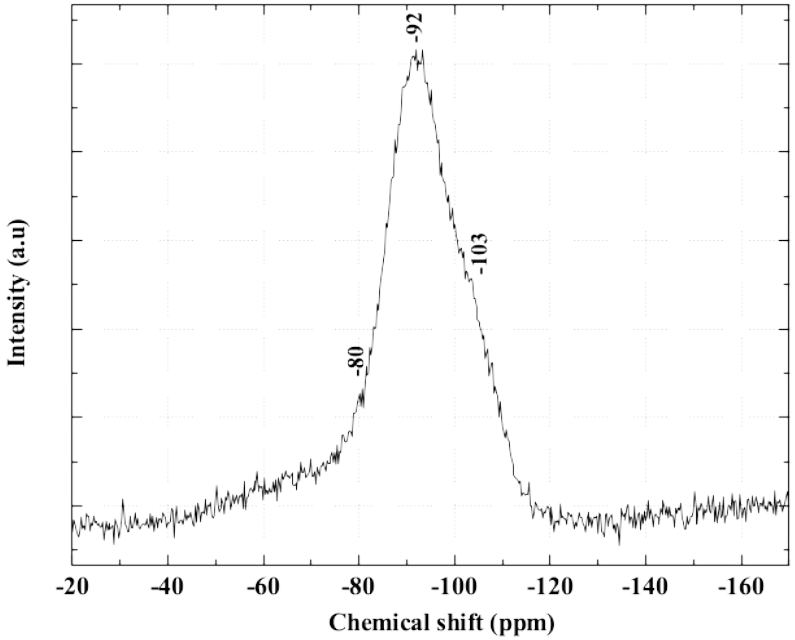


**Figure 6:** $^{29}$Si MAS-NMR spectrum of GP-125.

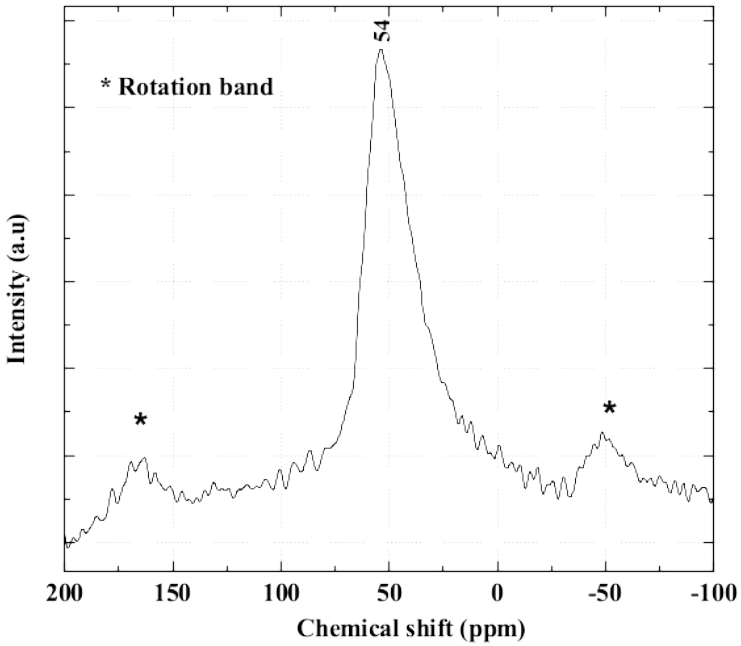


**Figure 7:** $^{27}$Al MAS-NMR spectrum of GP-125.

## 3. Characterization of the zeolitic products

### *3.1 Effect of GP particle size*

The XRD patterns of the recovered zeolitic products after hydrothermal treatment at 60°C for 6 days using various particle sizes (GP-63, GP-125 and GP-315) are represented in **figure 8.** For all patterns, one can see the peaks of Na-LTA zeolite ($|Na^{+}_{94.75}(H_2O)_{39.17}|$ $[Si_{96}Al_{96}O_{384}]$ (ICDD PDF No.01-089-8015) at 2θ angles 7.2°; 10.0°; 12.5°; 16.1°; 21.7°; 30.0°; 30.9°; 31.1°; 32.6°; 33.4° and 34.3°. Besides, we detected small amount of Na-P1 zeolite ($|Na^{+}_{6}(H_2O)_{12}|[Si_{10}Al_6O_{32}]$); ICDD PDF 01-071-0962) at 2θ angles 12.53°; 21.76°; 28.12° and 33.48°. Nevertheless, for **ZH-125-6d** and **ZH-315-6d** samples, there is small peaks around 6.2° and 11.6° 2θ which can be attributed to zeolite FAU X ($(|Na^{+}_{86}(H_2O)_{264}|[Si_{106}Al_{86}O_{384}]$ (ICDD PDF No. 38-0237). It is worth noting that for all samples there is broad hump between 15 and 35° 2θ which indicated the presence of amorphous material. The semi-quantitative phase analysis of the samples was accomplished with PANalytical X'Pert HighScore Plus (**table 2).** The results showed that the increase of GP particle size, the increase of zeolite Na-LTA quantity. Indeed, for Z**H-63-6d** sample the quantity of Na-LTA is about 73% while it is 93% for sample **ZH-315-6d.**

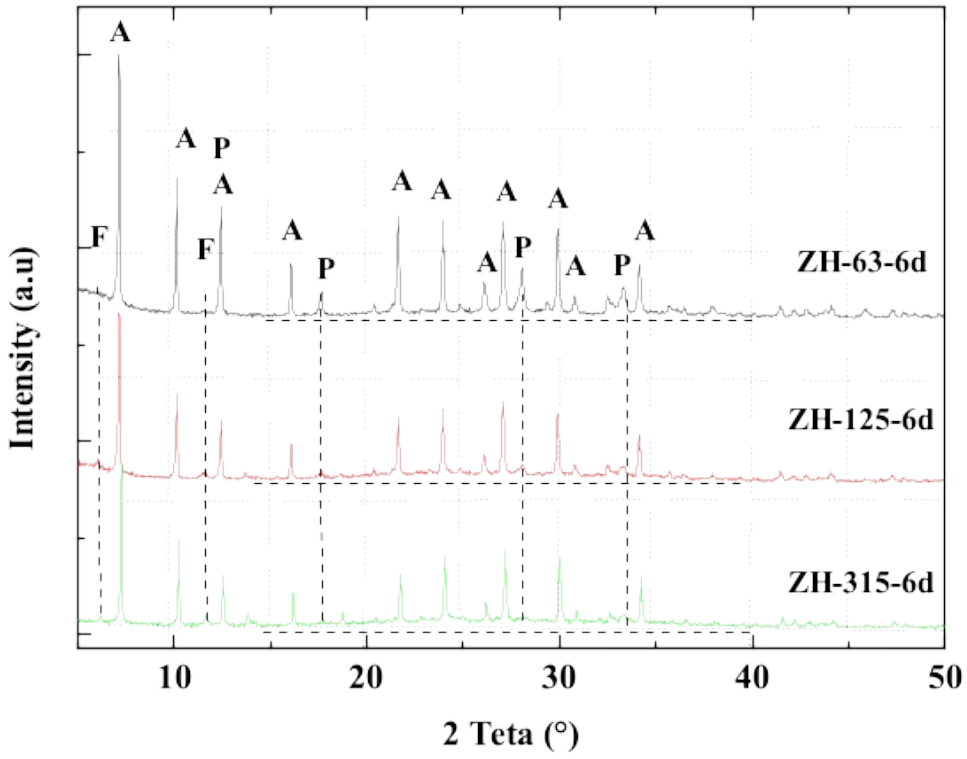


**Figure 8:** XRD patterns of zeolitic products ZH-63-6d, ZH-125-6d, and ZH-315-6d. Synthesis conditions (T(°C) = 60 ; t (days) = 6; S/L = 10 ; $m_{AS}$ (g) = 0.5).

**Table 2:** Semi-quantitative phase analysis of ZH-63-6d, ZH-125-6d and ZH-315-6d samples.

| Zeolite | JCPDS N° | ZH-63-6d | ZH-125-6d | ZH-315-6d |
|---|---|---|---|---|
| **Na-LTA (%)** | 01-073-2340 | 73 | 84 | 92 |
| **Na-P1 (%)** | 01-071-0962 | 27 | 16 | 8 |

The FTIR spectra of the solids recovered after hydrothermal treatment at 60°C for 6 days, ZH-63-6d, ZH-125-6d and ZH-315-6d are reported in **figure 9**. The spectra of the zeolitic products revealed important changes in relative intensities and width of the bands compared to GP spectrum. Hence, the band at 1040 $cm^{-1}$ attributed to asymmetric stretching vibration of Si- O- Si in the GP was moved to lower wavenumber at 1000-980 $cm^{-1}$ **[34, 65]**. This result confirms the destruction of GP structure and the formation of zeolite framework by linkage between $SiO_4$ and $AlO_4$ tetrahedra. Thus, the bands at around 1000-980 $cm^{-1}$ could be assigned to antisymmetric stretching of internal tetrahedral T–O bonds (T = Si or Al) in zeolites, whereas the symmetrical stretching ones are situated around 750 $cm^{-1}$. The bands near 675 $cm^{-1}$ are ascribed to a symmetric stretching of internal tetrahedra as well as of external linkages. Band near 460 $cm^{-1}$ was related to T-O bending mode in aluminosilicate zeolites. The bands located at around 560 $cm^{-1}$ are assigned to the vibrations of tetrahedra from external linkages of the double four rings (D4R) in the framework of zeolite Na-LTA **[66]**. The broad band at 3450 $cm^{-1}$ and the band at 1650 $cm^{-1}$ are associated to the stretching and bending modes of adsorbed water, respectively **[36]**. The bands at about 1454 $cm^{-1}$ can be assigned to C-O stretching in carbonate impurity.

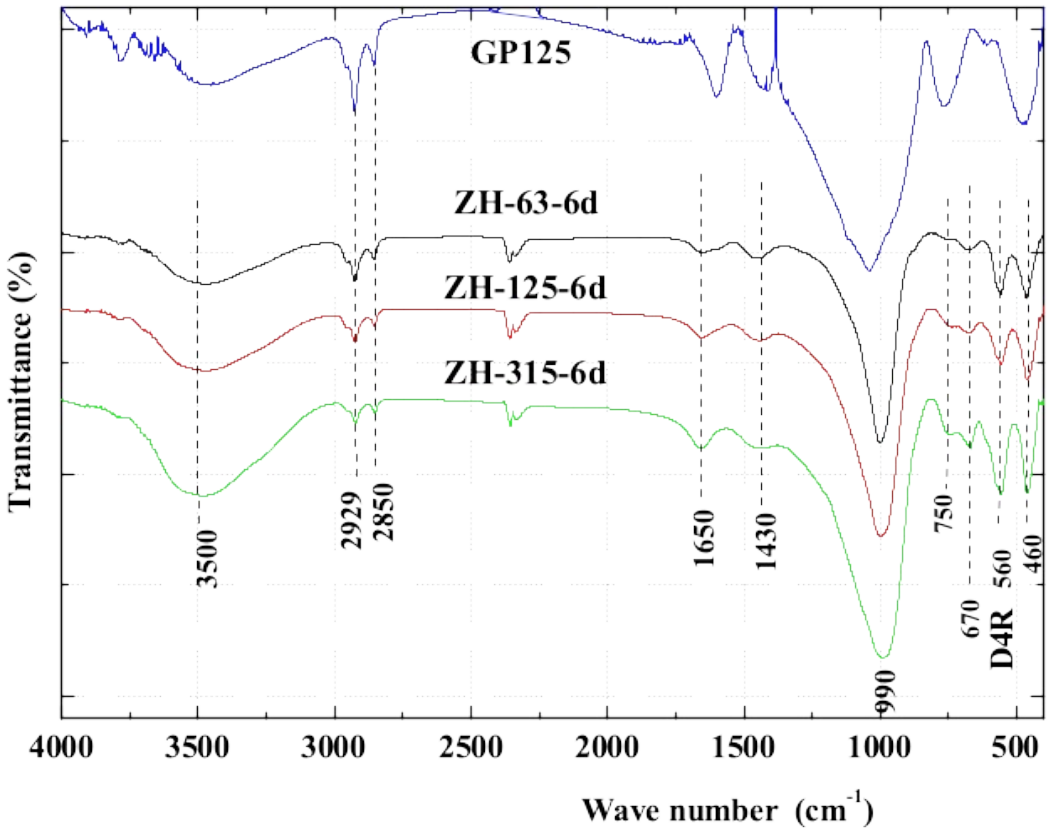


**Figure 9:** FTIR spectra of GP-125, ZH-63-6d, ZH-125-6d and ZH-315-6d samples. Synthesis conditions ( T(°C) = 60; t (days) = 6; S/L = 10 ; $m_{AS}$ (g) = 0.5 ).

The $^{27}$Al MAS-NMR spectra of **ZH-63-6d**, **ZH-125-6d** and **ZH-315-6d** products are illustrated in **figure 10**. All spectra exhibit one peak centered at 58 ppm which can be ascribed to the aluminum atoms in a tetrahedral coordination **[8, 9, 34, 64-65]**. It is worth mentioning that additional peaks were observed at around 9 ppm for **ZH-125-6d** and **ZH-315-6d** samples which may indicate the presence of another phase beside zeolite having the aluminum in octahedral environment.

**Figure 11** shows the $^{29}$Si MAS-NMR spectra of **ZH-63-6d**, **ZH-125-6d** and **ZH-315-6d** samples. All spectra have peaks with bad resolution laying between -110 and -80 ppm. Nevertheless, spectra of **ZH-63-6d** and **ZH-315-6d** showed mainly strong peak about –89 ppm and -90 ppm for **ZH-125-6d**. These peaks can be assigned to Si(4Al) and Si(3Al) of zeolite Na-LTA and Na-P1, respectively. Likewise, we detected low intensity peaks at -83, -86 and -94 ppm which could be attributed to Si(2Al), Si(1Al) and Si(0Al) of zeolite Na-P1 **[34, 66-67]**.

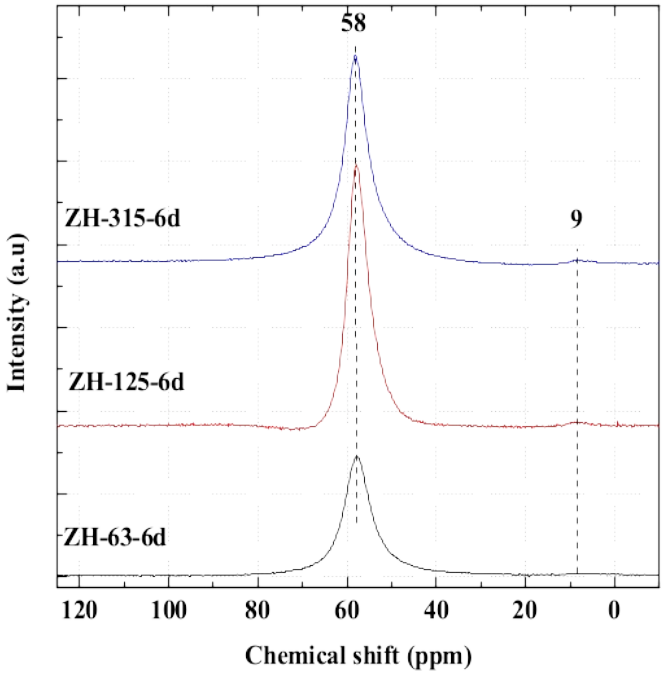


**Figure 10:** $^{27}$Al MAS NMR spectra of **ZH-63-6d**, **ZH-125-6d** and **ZH-315-6d**. Synthesis conditions (T(°C) = 60; t (days) = 6; S/L = 10 ; $m_{AS}$ (g) = 0.5 ).

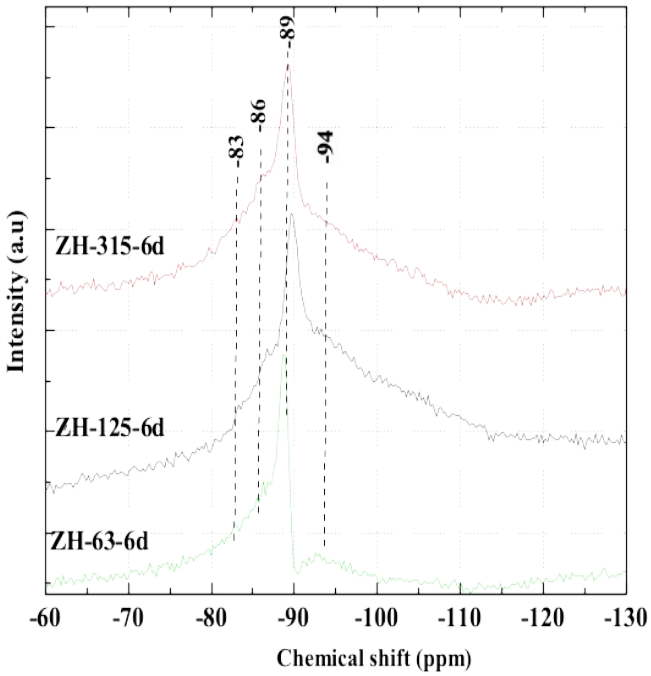

**Figure 11:** $^{29}$Si MAS NMR spectra of ZhH-125-6d, ZH-63-6d and ZH-315-6d. Synthesis conditions (T(°C) = 60; t (days) = 6; S/L = 10 ; $m_{AS}$ (g) = 0.5 ).

The $N_2$ adsorption/desorption isotherms of samples Zh-125-6d, Zh-63-6d and, Zh-315-6d are reported in **figure 12**. The BET surface area ($S_{BET}$), micropore volume (μV), micropore surface (μS) and pore diameter ($Ø_{pore}$) of the samples are summarized in **Table 3**. It should be mentioned that the GP is non-porous. The adsorptions isotherms of the three samples did not clearly display the expected type I isotherm, ascribed to microporous zeolites. Nevertheless, they can be classified as types between II–IV according to the IUPAC classification **[68].** We note that for very low relative pressures ($P/P^0$ < 0.02), there is an increase in nitrogen adsorption attributed to the filling of the some micropores. The amount of adsorbed nitrogen increases steadily from 0.02 to 0.4 $P/P^0$, resulting in the formation of a monolayer followed by multilayer. For relative pressures 0.4 and 0.98 $P/P^0$, we noticed the appearance of hysteresis loops which differ in their sizes. The presence of hysteresis loops is due to capillary condensation of nitrogen in intercrystal mesopores arising from the packing of zeolite crystals **[35]**. At the relative pressure of 0.9 to 0.98 $P/P^0$, the adsorption branch and the desorption branch rapidly increased and coincided at the end. The large adsorption amount at $P/P^0$ > 0.9 shows the presence of macropores (d > 50 nm) in the samples. Hysteresis loops of the samples belong to type H3, along with a small amount of type H4 **[69].** Type H3 is attributed to wedge-shaped pores formed by the loose stacking of flaky particles, and Type H4 is a result of slit-shaped pores resulting from internal parallel pore structure **[70]**.

On the other hand, there is a decrease of $S_{BET}$ surface area by increasing GP particle size. This behavior can be related to the relative quantities of zeolites in each sample. According to Table 1, sample **ZH-315-6d** which contains 97 wt.% of Na-LTA zeolite has the lowest BET surface area (3 $m^2/g$), whereas for sample **ZH-63-6d** which formed of 73 wt.% of Na-LTA, the BET surface area become 61 $m^2/g$. This phenomenon is related to the structure of zeolites Na-LTA and Na-P1. For zeolite Na-LTA, the presence of $Na^+$ cations near octagonal openings (Φ = 4.2 Å) prevents the diffusion of nitrogen molecules (Φ = 4.54 Å) in the zeolite framework **[1]**. Abid et al. **[32]** prepared from AS and industrial metasilicate pure zeolite Na-LTA with $S_{BET}$ = 10.8 $m^2/g$. The exchange of Na-LTA with $Ca^{2+}$ cations modified the pore diameter from 4 Å to 5 Å which increased the $S_{BET}$ from 10.8 $m^2$ /g to = 550.0 $m^2$ /g.

For zeolite Na-P1, the main window dimension of the channel is about 3.1 × 4.5 Å which is not accessible for nitrogen. Nevertheless, its structure is flexible and has good ion exchange properties. This performance is attributed to the small crystallite sizes with large external surface areas.

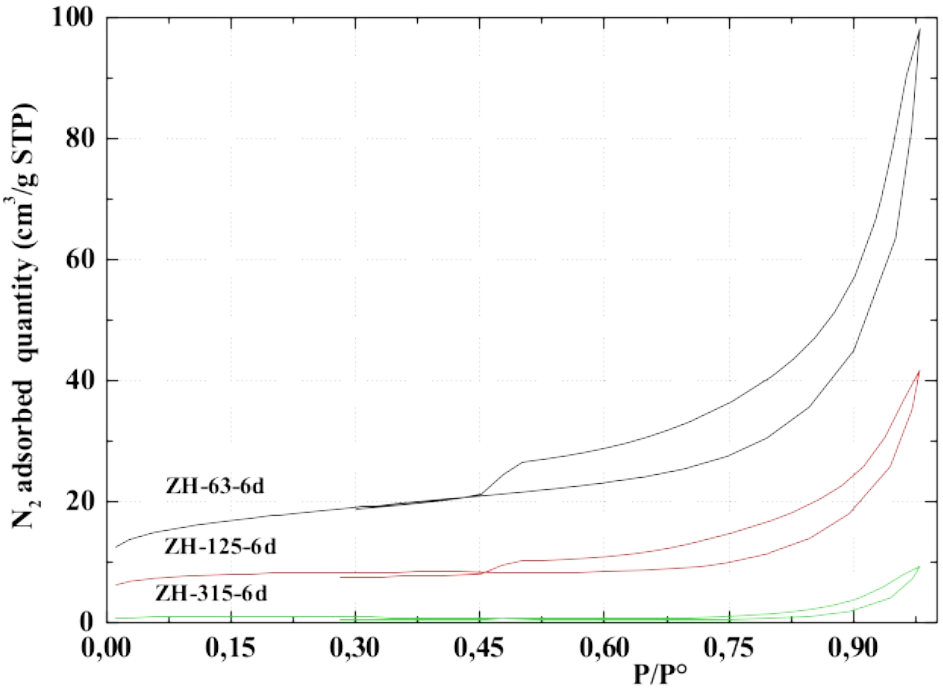


**Figure 12:** $N_2$ adsorption–desorption isotherms of ZH-63-6d, ZH-125-6d and ZH-315-6d samples. Synthesis conditions (T(°C)= 60; t (days) = 6; S/L = 10 ; $m_{AS}$ (g) = 0.5).

**Table 3:** BET surface area (SBET), micropore surface area (µS), micropore volume (µV) and pore diameter ($Ø_{pore}$) of ZH-63-6d, ZH-125-6d and ZH-315-6d samples.

| Samples | $S_{BET}$ ($m^2/g$) | µS ($m^2/g$) | µV ($cm^3/g$) | $Ø_{pore}$ (nm) |
|---|---|---|---|---|
| **ZH-63-6d** 27% Na-P1 | 61 | 24 | 0.137 | 10.9 |
| **ZH-125-6d** 16% Na-P1 | 27 | 19 | 0.055 | 10.8 |
| **ZH-315-6d** 8% Na-P1 | 3 | 3.8 | 0.012 | 15.9 |

### *3.2 Effect of crystallization time*

The XRD patterns of the zeolitic products obtained from **GP-125** after hydrothermal crystallization at 60 °C after different crystallization periods are illustrated in **figure 13**. It is clear that the main product is the zeolite Na-LTA ($|Na^+_{96}(H_2O)_{216}|[Si_{96}Al_{96}O_{384}]$), JCPDS No. **01-073-2340)**. After 2 days of crystallization, small peaks relating to Na-LTA zeolite overcoming the amorphous phase appeared. The increase of crystallization period from 2 to 6 days increases the

peak intensities of Na-LTA zeolite. Nevertheless, from 4 to 10 days small quantities of Na-P1 zeolite ($|Na^{+}_{6}(H_2O)_{12}|[Si_{10}Al_6O_{32}]$), JCPDS No. **01-071-0962** were detected. On the other hand, the broad hump between 15 and 35° 2θ in the patterns of the zeolitic products indicated the presence of amorphous material. The formation of Na-P1 zeolite can be explained by the transformation of the metastable zeolite Na-LTA to more thermodynamically stable zeolite Na-P1 at longer reaction time. This result illustrates Oswald's rule of successive transformations; the nucleation and crystallization of the new phase occurs in the supersaturared solution throughout the dissolution of the former phase **[2]**.

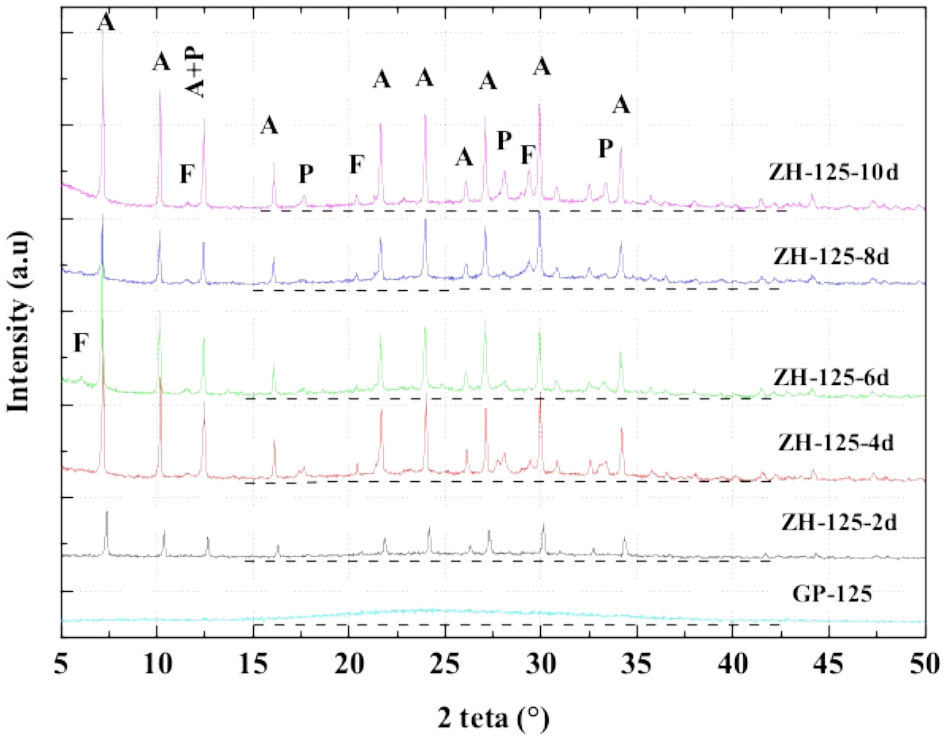


**Figure 13:** XRD patterns of zeolitic products obtained after hydrothermal treatment of **GP-125** at different crystallization periods (2, 4, 6, 8 and 10 days). Synthesis conditions (T(°C) = 60; Ø(μm) <125; S/L = 10 ; $m_{AS}$ (g) = 0.5 ).

The SEM micrographs of the zeolitic products obtained from **GP-125** after hydrothermal crystallization at 60 °C for different crystallization periods are illustrated in **figure 14.** The SEM micrograph of sample ZH-125-2d (**figure 14b)** showed porous surface on which particles of indefinite morphology are deposited. This porous surface is the result of the dissolution of the glass particle in the alkaline medium. After 4 days of hydrothermal crystallization (ZH-125-4d sample),

one can see a layer of gel covering the porous glass fragments and a roughly cubic-shaped growing zeolite crystals. After 6 days, the cubic morphology of Na-LTA zeolite of ZH-125-6d sample is well pronounced. After 8 days, micrograph of sample depicted. After 8 days, the SEM micrograph of the sample ZH-125-8d shows crystals of poorly defined morphology deposited on a fragment of porous glass. It seems that the crystals of Na-LTA zeolite begun to dissolve.

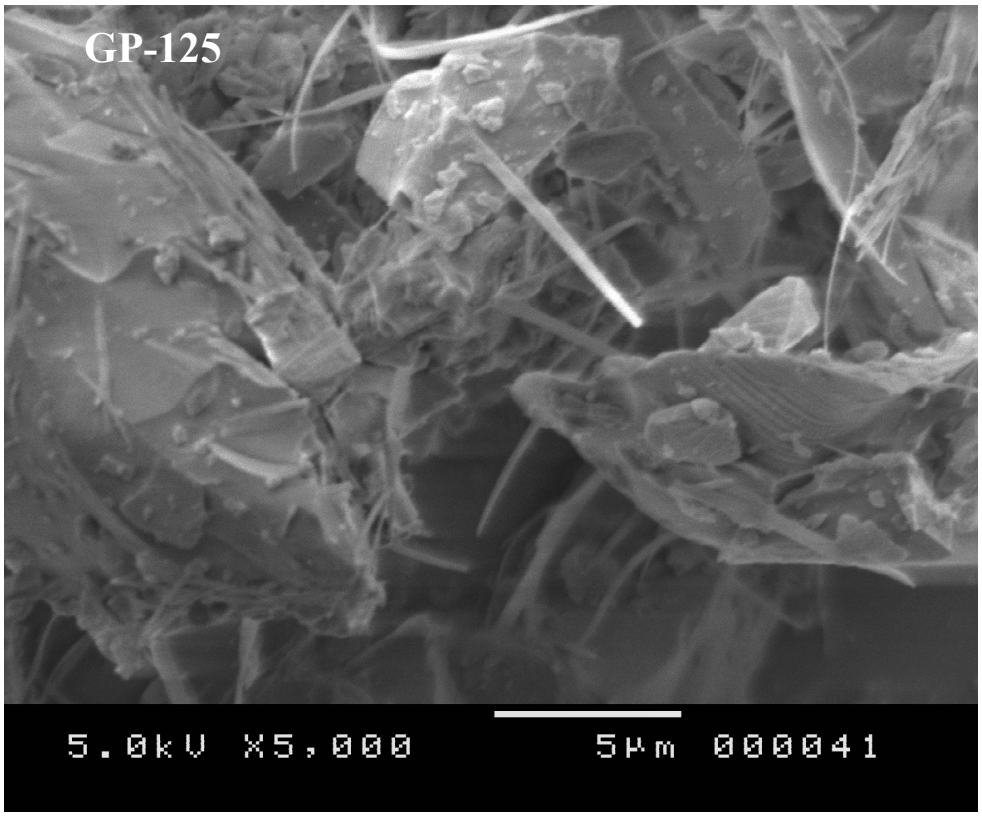

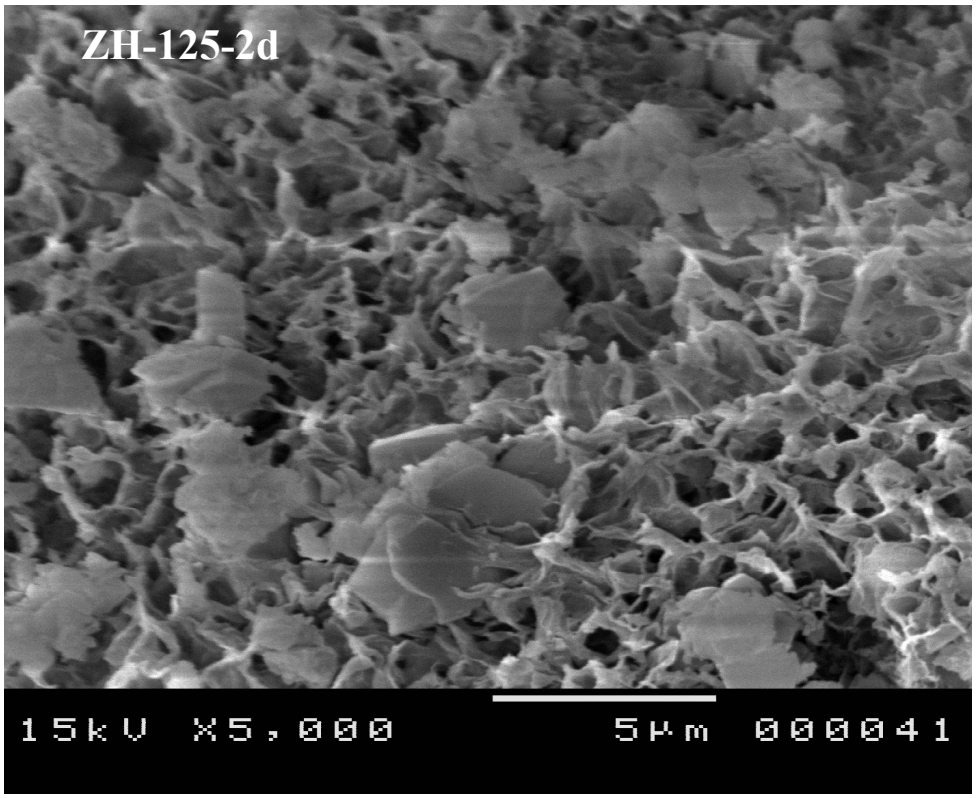
ZH-125-2d
15kV X5,000 5µm 000041

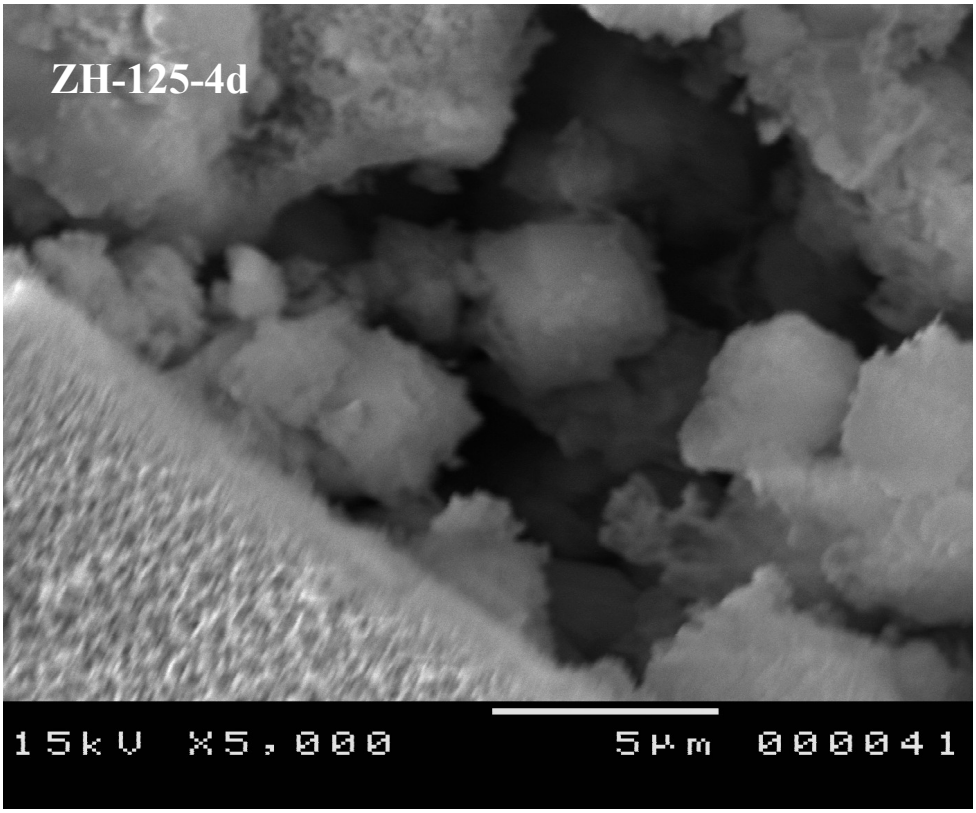
ZH-125-4d
15kV X5,000 5µm 000041

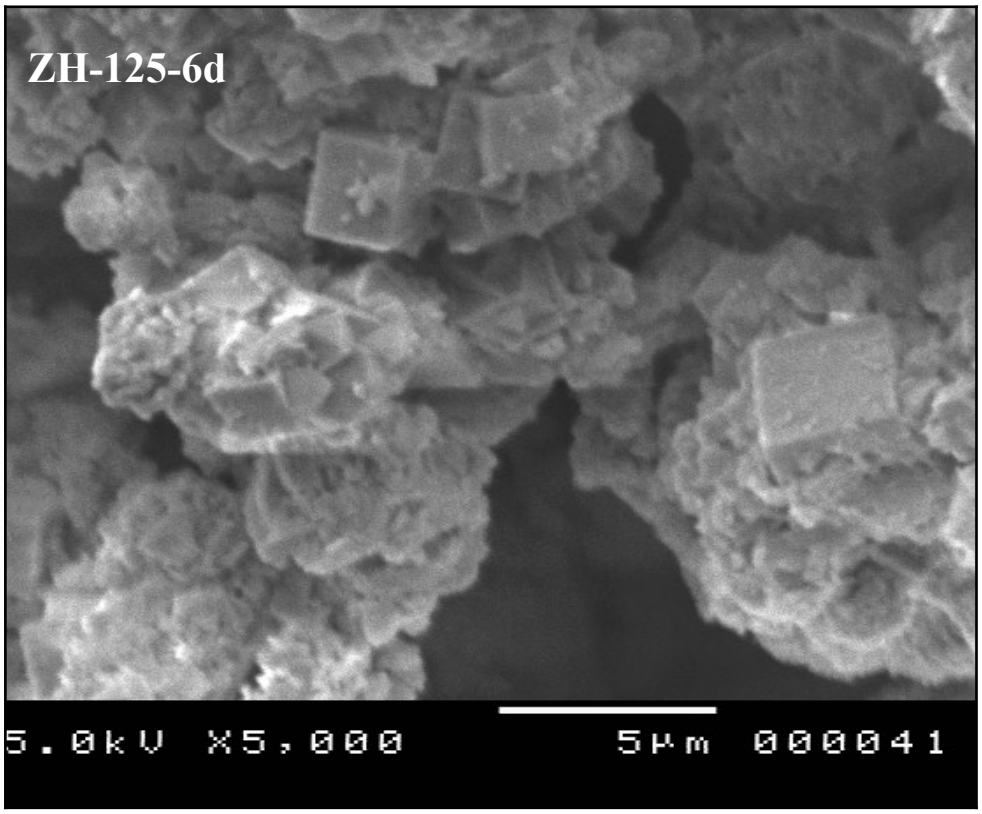


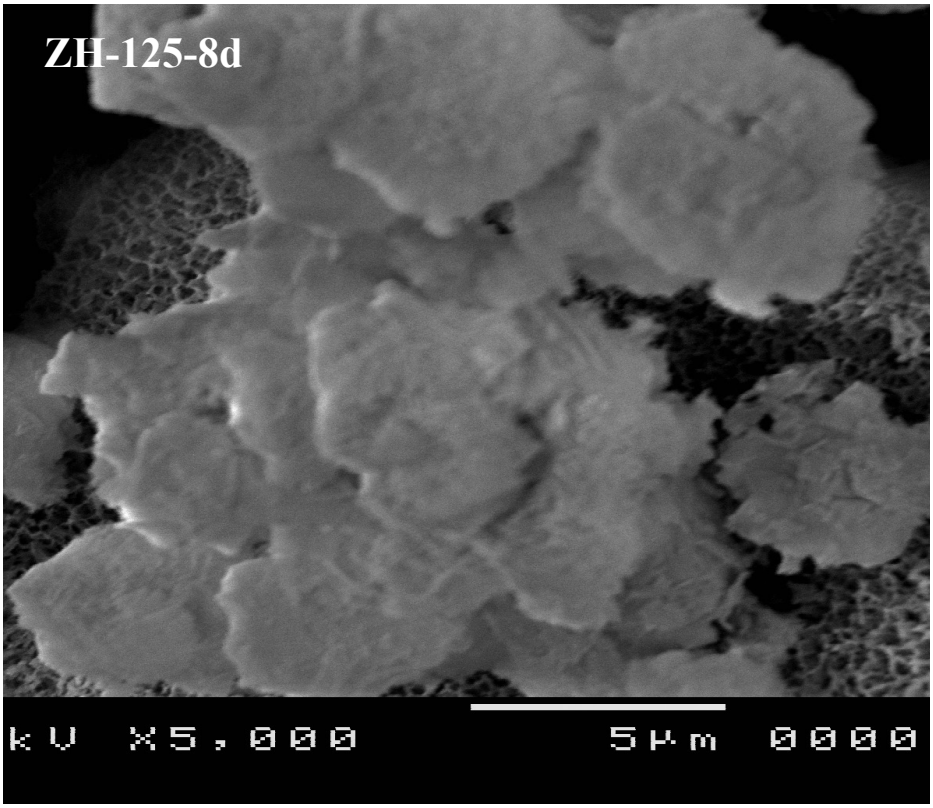


**Figure 14:** SEM micrographs of GP-125, ZH-125-2d, ZH-125-4d, ZH-125- 6d and ZH-125- 8d. Synthesis conditions (T(°C)= 60; Ø (µm) <125; S/L = 10 ; $m_{AS}$ (g) = 0.5 ).

### *3.3 Effect of AS quantity*

**Figure 15** exhibits the XRD profiles of the zeolitic products recovered after 6 days of hydrothermal treatment at 60 °C as function of AS quantity. **Table 4** illustrated the $SiO_2/Al_2O_3$ ratios of the reaction mixtures before hydrothermal synthesis. It is worth noting that for all samples there is broad hump between 15 and 35° 2θ which indicated the presence of amorphous material. The use of a small amount of AS (ZH-125-Al-0.125) resulted in the appearance of FAU type structure with low intensity reflexes contaminated with Na-P1 and Na-LTA zeolites. The increase of the amount of AS (ZH-125-0.25g, ZH-125-0.5g, ZH-125-0.75g) promotes the formation of LTA zeolite and enhanced the peak intensities. The further increase of AS (ZH-125-Al-1.0) there is apparition of hydoxysodalite zeolite HS ($|Na^+_8(H_2O)_8|[Si_6Al_6O_{24}]$ ICDD PDF No.11-0401) at angles 14.01°, 24.38°, and 35.60° 2θ in addition to Na-LTA, FAU and Na-P1 zeolites. It appears that the increase of the quantity of AS in the synthesis mixture (decrease of $SiO_2/Al_2O_3$ ratio) leads to the gradual decrease in the Si/Al ratio of zeolite and favors the crystallization of the Na-LTA zeolite (Si/Al=1.0). On the other hand, the decrease of the quantity of AS favors the crystallization of faujasite zeolite ($1.0 < Si/Al \leq 1.5$).

**Table 4:** $SiO_2/Al_2O_3$ molar ratios of the reaction mixtures before hydrothermal synthesis.

| AS quantity (g) | 0.125 | 0.25 | 0.5 | 0.75 | 1.0 |
|---|---|---|---|---|---|
| $SiO_2/Al_2O_3$ | 2.2 | 1.54 | 1.11 | 0.66 | 0.52 |

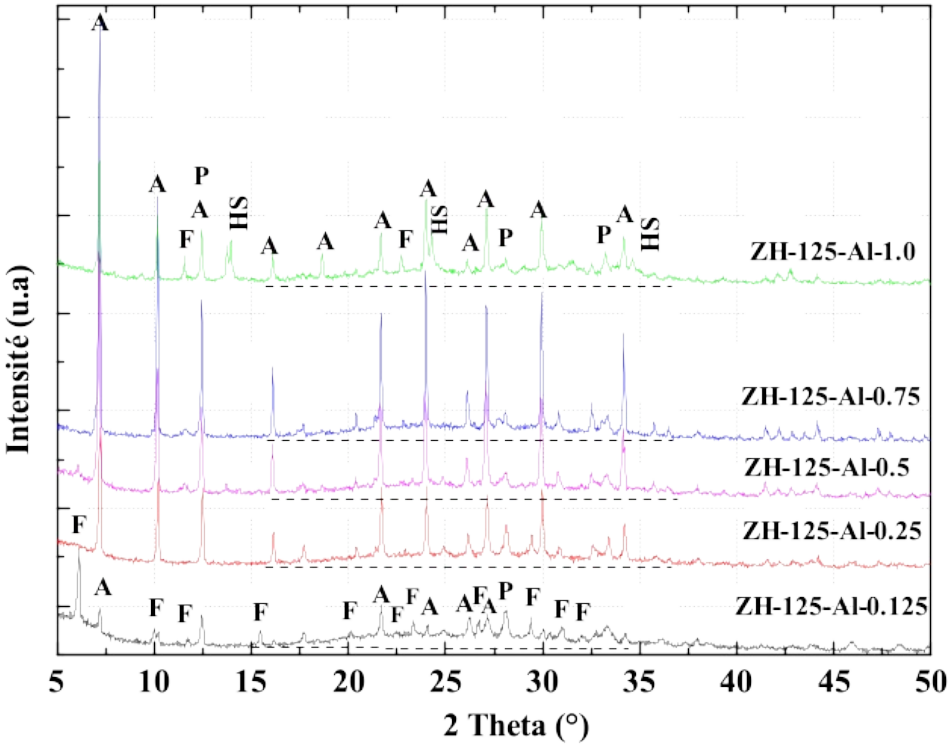


**Figure 15:** XRD patterns of products obtained after hydrothermal treatment of **GP-125** using different AS amounts. Synthesis conditions (T(°C) = 60; t (days) = 6; Ø(µm) <125; S/L = 10 ).

### *3.4 Effect of liquid/solid ratio*

The XRD profiles of the solids recovered after hydrothermal treatment of GP at 60°C for 6 days and varying the L/S ratios are depicted in **Figure 16.** For low water content, XRD pattern of **ZH-125-6d-5** showed the peaks of Na-LTA zeolite contaminated with small quantity of Na-P1 zeolite. The peak intensities of zeolite Na-LTA are enhanced with the increase of water content till L/S ratio become equal to 15. The further increase causes a drastic decrease of peak intensities of **ZH-125-6d-20**. For sample **ZH-125-6d-10,** one can see the presence of tiny amount of faujasite zeolite (peak at 6.1° 2θ) besides Na-LTA and Na-P1. The increase of water content dilutes the reaction mixture, drops the concentration of the primary species which decreases the rate of nucleation and finally slows down the rate of crystallization and reduces the crystallinity of Na-LTA **[71]**.

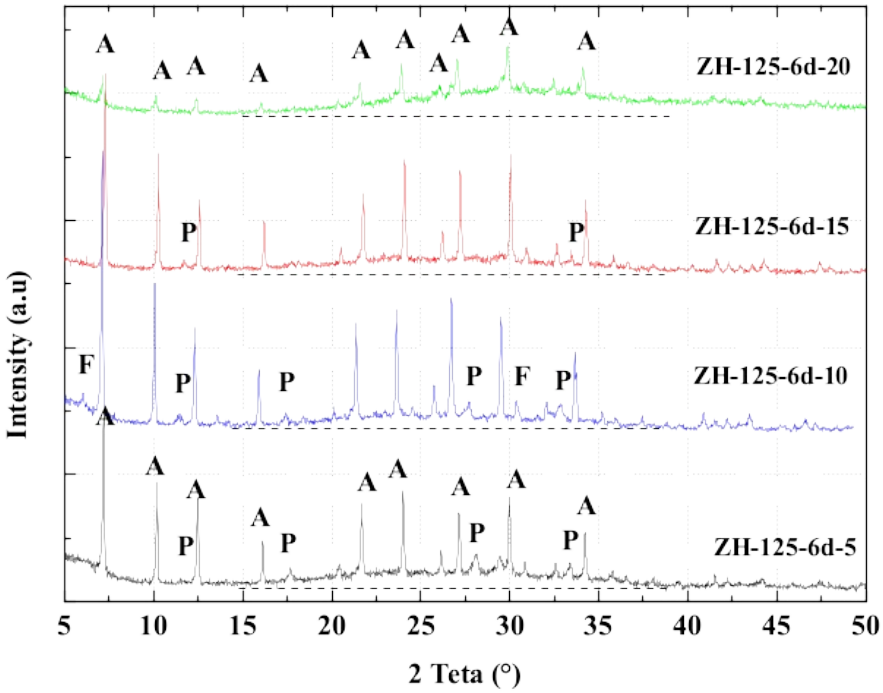


**Figure 16:** XRD patterns of zeolitic products obtained after hydrothermal treatment at 60 °C for 6 days of **GP-125** using different L/S ratios. Synthesis conditions (T (°C) = 60; t (days) = 6; Ø (μm) <125; $m_{AS}$ (g) = 0.5).

### *3.5 Discussion*

The zeolitization mechanism of GP under mild hydrothermal treat- ment (T = 60 ◦ C) can be divided into three steps: dissolution, nucleation and growth mechanism. The dissolution of the amorphous structure of the GP is the key step in the formation of zeolites. Indeed, the reaction of GP with the alkaline solution leads to the hydrolysis of Si-O-Si bonds by the formation of silanol groups (Si-OH) on the surface of GP and sodium silicate in solution **[61]**. The dissolution reaction depends on the tem- perature, the concentration of OH- ions, the L/S ratio, and the particle of the GP. Nevertheless, the glass network hydrolysis is more rapid when non-bridging oxygen atoms were present. Site reactivity followed the trend Q1 > Q2 > Q3 > Q4 as reported by Kouassi et al. **[61]**. In our case, the hydrolysis of Si-O-Si and probably Si-O-Al of GP gives rise to silica monomers [SiO(OH)3]- and -[SiO2(OH)2]2- and a small amount- of aluminate monomers Al(OH)4 (the remaining amount of Al(OH)4 is provided by the dissolution of AS). As a result, the reactive precursors condensed to form an aluminosilicate gel. The condensation of aluminate and silicate species is governed by the Si/Al ratio. For Si/Al= 1, a rapid condensation occurs between the

aluminate ions and the silicate species. On the other hand, for Si/Al> 1, the silicate species tend to build up silicate oligomers ([Si2O3(OH)4]2-, [Si3O5(OH)5]3- and [Si4O8(OH)4]4-) for pH values ≥ 10 **[72]** which in turn condense with the aluminate monomers to form aluminosilicate gel. Maintained at 60 ◦C, the gel is constantly changing; some parts dissolve, others organize themselves differently. More stable combinations such as secondary building (S4R, S6R, D4R, D6R...) and tertiary building units (beta cage) are formed and tend to become predominant and which are capable of reacting with each other to form critical nuclei of the product phase large enough to have the ability to grow irreversibly. After nucleation, there is incorporation of aluminosilicate units onto the surface of the crystal causing a growth of the size. In this step, a series of transitory thermodynamically-metastable intermediate phases evolves according to the Ostwald Law of successive transformations can be observed **[2]**. The initial precipitation of Na-LTA and its subsequent conversion to Na-P1 is observed in the present study. According to the SEM technique, the majority of the zeolitic materials are located on the external surface of GP waste. Nevertheless, zeolite crystals can be developed between the waste fragments.

## 4. Conclusion

The conversion of waste glass and aluminum scraps into zeolites could contribute to the enhancement of waste utilization in a high-value application. In this work, the synthesis of zeolites from waste glass and aluminum scarps was attempted through hydrothermal treatment without pretreatment. The synthesis was controlled by many factors such as hydrothermal time, particle size, aluminum concentration and solid /liquid. The Zeolithization of the solid waste at 60 ◦C for 6 days allowed us to prepare a mixture of Na-LTA and Na-P1 type zeolites. The reduction in the size of glass waste powder promotes the formation of the Na-P1 zeolite, which is richer in silicon, at the expense of the Na-LTA zeolite. The zeolite kinetics showed that from 2 days of crystallization the amorphous phase of the glass waste disappeared and peaks charac- teristic of LTA zeolite appear. After 4 days, in addition to the LTA zeolite, it was noticed that the intensities of the NaP1 zeolite appear and grad- ually increase. This can be explained by the transformation of the metastable phase (Na-LTA zeolite) to a thermodynamically more stable phase (Na-P1). It is well known that zeolite formation is a kinetically controlled process and the reaction is usually stopped when the desired zeolite formed. The decrease in the amount of aluminum promotes the synthesis of FAU zeolite. The study of the effect of the liquid/solid ratio showed that well crystallized LTA zeolite was obtained with a liquid/ solid ratio equal to 10. The advantage of this study is the recovery of glass and aluminum waste into zeotype materials of high added value and to prevent our environment from non-degradable solid waste type pollutants.

## References

**[1]** D.W. Breck, Zeolite Molecular Sieves: Structure, Chemistry and Use, John Wiley & Sons Inc, New York, NY, 1974.

**[2]** C.S. Cundy, P.A. Cox, The hydrothermal synthesis of zeolites: precursors, intermediates and reaction mechanism, Microporous Mesoporous Mater. 82 (1–2) (2005) 1–78.

**[3]** M. Kro´l, Natural vs. synthetic zeolites, Crystals 10 (2020) 622.

**[4]** F. Collins, A. Rozhkovskaya, J.G. Outram, G.J. Millar, A critical review of waste resources, synthesis, and applications for Zeolite LTA, Microporous Mesoporous Mater. 291 (2020), 109667.

**[5]** L.F. de Magalh˜aes, G.R. da Silva, A.E.C. Peres, Zeolite application in wastewater treatment, Hindawi Adsorpt. Sci. Technol. Volume (2022) 26. Article ID 4544104.

**[6]** R.Jarosz,J.Szerement,K.Gondek,M.Mierzwa-Hersztek,The use of zeolites as an addition to fertilisers – a review, Catena 213 (2022), 106125.

**[7]** S.M. Al-jubouri, B.I. Waisi, S.M. Holmes, Rietveld texture refinement analysis of linde type A zeolite from x-ray diffraction data", Eng. Sci. Technol. 13 (2018) 4066–4077.

**[8]** H. Tounsi, S. Mseddi, S. Djemal, Hydrothermal synthesis of Na-LTA, Na-X and HS zeolites from Tunisian sand and aluminum scraps, Mater. Sci. Forum 636–637 (2010) 1389–1396, https://doi.org/10.4028/www.scientific.net/MSF.636- 637.1389.

**[9]** H.Tounsi,S.Mseddi,S.Djemel, Preparation and characterization of Na-LTA zeolite from Tunisian sand and aluminum scrap, Phys. Procedia 2 (2009) 1065–1074.

**[10]** I.V. Joseph, L. Tosheva, G. Miller, A.M. Doyle, FAU-type zeolite synthesis from clays and its use for the simultaneous adsorption of five divalent metals from aqueous solutions, Materials 14 (2021) 3738, https://doi.org/10.3390/ ma14133738.

**[11]** M.Tavasoli,H.Kazemian,S.Sadjadi,M.Tamizifar, Synthesis and characterization of zeolite NaY using kaolin with different synthesis methods, Clays Clay Miner. 62 (2014) 508–518.

**[12]** N. Belachew, H. Hinsene, Preparation of zeolite 4A for adsorptive removal of methylene blue: optimization, kinetics, isotherm, and mechanism study, Silicon 14 (2022) 1629–1641.

**[13]** K.K. Salam, E.O. Oke, C.J. Ude, U. Yahaya, Zeolite-Y-based catalyst synthesis from Nigerian Elefun Metakaolin: computer-aided batch simulation, comparative predictive response surface and neuro-fuzzy modelling with optimization, Chem. Pap. 76 (2022) 1213–1224.

**[14]** X. Lu, L. Liu, H. Liu, G. Tian, G. Peng, L. Zhuo, Z. Wang, J. Taiwan, Zeolite-X synthesized from halloysite nanotubes and its application in CO2 capture, Inst. Chem. Eng. 133 (2022), 104281.

**[15]** D. Gandhi, R. Bandyopadhyay, B. Soni, Zeolite Y from kaolin clay of Kachchh, India: synthesis, characterization and catalytic application, J. Indian Chem. Soc. 98 (12) (2021), 100246.

**[16]** Y. He, S. Tang, S. Yin, S. Li, Research progress on green synthesis of various high- purity zeolites from natural material-kaolin, J. Clean. Prod. 306 (2021), 127248.

**[17]** M. Rubtsova, E. Smirnova, S. Boeva, et al., Nanoarchitectural approach for synthesis of highly crystalline zeolites with a low Si/Al ratio from natural clay nanotubes, Microporous Mesoporous Mater. 330 (2022), 111622.

**[18]** E. Gagliano, M. Sgroi, P.P. Falciglia, C. Belviso, F. Cavalcante, A. Lettino, F.G., A. Vagliasindi, Paolo Roccaro, Removal of ammonium from wastewater by zeolite synthetized from volcanic ash: Batch and column tests, Engineering 10 (3) (2022), 107539.

**[19]** Y. Cheng, L. Xu, C. Liu, NaP1 zeolite synthesized via effective extraction of Si and Al from red mud for methylene blue adsorption, Adv. Powder Technol. 32 (10) (2021) 3904–3914.

**[20]** D. Zhao, A. Armutlulu, Y. Chen, Yinxu Wang, R. Xie, Highly efficient removal of Cu (II) using mesoporous sodalite zeolite produced from industrial waste lithium- silicon-fume via reactive oxidation species route, J. Clean. Prod. 319 (2021), 128682.

**[21]** C. Miao, L. Liang, F. Zhang, S. Chen, K. Shang, J. Jiang, Y. Zhang, J. Ouyang, Review of the fabrication and application of porous materials from silicon-rich industrial solid waste, Int. J. Miner. Met. 29 (3) (2022) 424, https://doi.org/ 10.1007/s12613-021-2360-9.

**[22]** P. Sirinwaranon, V. Sricharoenchaikul, D. Atong, Catalytic performance of Co, Fe on MCM-41 synthesized from illite waste for gasification of torrefied cassava rhizome, Energy Rep. 7 (2021) 149–162.

**[23]** X. Zhang, C. Li, S. Zheng, Y. Di, Z. Sun, A review of the synthesis and application of zeolites from coal-based solid wastes, Int. J. Miner. Metall. 29 (1) (2022) 1.

**[24]** N. Sazali, Z. Harun, T. Abdullahi, N.H. Kamarudin, N. Sazali, M.R. Jamalludin, S.K. Hubadillah, S.S. Alias, The route of hydrothermal synthesis zeolite□A from the low□grade perak kaolin, Malaysia, Silicon (2022), https://doi.org/10.1007/ s12633-021-01620-4.

**[25]** A. Khaleque, M.M. Alam, M. Hoque, et al., Zeolite synthesis from low-cost materials and environmental applications: A review, Environ. Adv. 2 (2020), 100019.

**[26]** M. Yoldi, E.G. Fuentes-Ordon ˜ez, S.A. Korili, A. Gil, Zeolite synthesis from industrial wastes, Microporous Mesoporous Mater. 287 (2019) 183–191.

**[27]** A. Lopez-Delgado, J.I. Robla, I. Padilla, S. Lopez-Andres, M. Romero, Zero-waste process for the transformation of a hazardous aluminum waste into a raw material to obtain zeolites, J. Clean. Prod. 255 (2020), 120178.

**[28]** A. Hernandez-Palomares, F. Espejel-Ayala, Precipitated silica, alkali silicates and zeolites from construction and demolition waste materials, J. Clean. Prod. 348 (2022), 131346.

**[29]** Y. Jin, L. Li, Z. Liu, S. Zhu, D. Wang, Synthesis and characterization of low-cost zeolite NaA from coal gangue by hydrothermal method, Adv. Powder Technol. 32 (2021) 791–801.

**[30]** M.M. Kumara, H. Jena, Direct single-step synthesis of phase pure zeolite Na–P1, hydroxy sodalite and analcime from coal fly ash and assessment of their Cs+ and Sr2+ removal efficiencies, Microporous Mesoporous Mater. 333 (2022), 111738.

**[31]** K. Vegere, R. Kravcevica, A.E. Krauklis, T. Juhna, Comparative study of hydrothermal synthesis routes of zeolite A, Mater. Today Proc. 33 (Part 4) (2020) 1984–1987, https://doi.org/10.1016/j.matpr.2020.06.326.

**[32]** R. Abid, G. Delahay, H. Tounsi, Selective catalytic reduction of NO by NH3 on cerium modified faujasite zeolite prepared from aluminum scraps and industrial metasilicate, J. Rare Earths 38 (2020) 250–256.

**[33]** M. Sayehi, H. Tounsi, G. Garbarino, P. Riani, G. Busca, Reutilization of silicon- and aluminum-containing wastes in the perspective of the preparation of SiO2-Al2O3 based porous materials for adsorbents and catalysts, Waste Manag. 103 (2020) 146–158.

**[34]** M. Sayehi, G. Garbarino, G. Delahay, G. Busca, H. Tounsi, Synthesis of high value- added Na-P1 and Na-FAU zeolites using waste glass from fluorescent tubes and aluminum scraps, Mater. Chem. Phys. 248 (2020), 122903.

**[35]** M. Sayehi, S. Hajji, L. Boudjema, H. Kazemian, M. Nasri, H. Tounsi, Using a zeolite produced from glass waste and aluminum scraps to develop a novel gelatin-based biodegradable composites films: antibacterial and antioxidant properties of a potential food packaging material, Inorg. Chem. Commun. 140 (2022), 109415.

**[36]** N. Maatoug, G. Delahay, H. Tounsi, Valorization of vitreous China waste to EMT/ FAU, FAU and Na-P zeotype materials, Waste Manag. 74 (2018) 267–278.

**[37]** R. Abid, G. Delahay, H. Tounsi, Preparation of LTA, HS and FAU/EMT intergrowth zeolites from aluminum scraps and industrial metasilicate, J. Mater. Cycles Waste Manag. 21 (2019) 1188–1196.

**[38]** M. Noviello, C.E. Gattullo, I. Allegretta, R. Terzano, G. Gambacorta, V.M. Paradiso, Synthetic zeolite materials from recycled glass and aluminum food packaging as potential oenological adjuvant, Food Packag. Shelf Life 26 (2020), 100572.

**[39]** J. Gupta, A.S. Jethoo, P.V. Ramana, Valorization of soda lime glass in cement sand matrix. Mater. Today Proc. (2022).

**[40]** J.H. Taylor, V.K. Elmes, A.P. Hurt, N.J. Coleman, Synthesis of feldspathoids and zeolite K–F from waste amber container glass, Mater. Chem. Phys. 246 (2020), 122805.

**[41]** M. Roulia, K. Koukouza, M. Stamatakis, C. Vasilatos, Fly-ash derived Na-P1, natural zeolite tuffs and diatomite in motor oil retention, Clean Mater. 4 (2022), 100063.

**[42]** Y.-J. Lin, J.-C. Chen, Resourcization and valorization of waste incineration fly ash for the synthesis of zeolite and applications, J. Environ. Chem. Eng. 9 (6) (2021), 106549.

[43] [44]

[45]

[46] [47] [48]

[49] [50] [51] [52] [53]

[54] [55] [56] [57]

[58]

[59]

[60]

[61] [62]

[63] [64]

[65]

[66] [67]

[68]

[69] [70]

**[43]** Z. Tauanov, S. Azat, A. Baibatyrova, A mini-review on coal fly ash properties, utilization and synthesis of zeolites, Int. J. Coal Prep. Util. (2020), https://doi.org/ 10.1080/19392699.2020.1788545.

**[44]** S.M. Al-jubouri, S.I. Al-batty, S.M. Holmes, Using the ash of common water reeds as a silica source for producing high purity ZSM-5 zeolite microspheres, Microporous Mesoporous Mater. 316 (2021), 110953, https://doi.org/10.1016/j. micromeso.2021.110953.

**[45]** S.M. Al-jubouri, S.I. Al-batty, S. Senthilnathan, N. Sihanonth, Utilizing Faujasite- type zeolites prepared from waste aluminum foil for competitive ion-exchange to remove heavy metals from simulated wastewater, Desalin. Water Treat. 231 (2021) 27461, https://doi.org/10.5004/dwt.2021.

**[46]** F. García-Vill´en, E. Flores-Ruíz, C. Verdugo-Escamilla, F.J. Huertas, Hydrothermal synthesis of zeolites using sanitary ware waste as a raw material, Appl. Clay Sci. 160 (2018) 238–248.

**[47]** J. Maisuria, V.K. Elmes, A.P. Hurt, A.A. Coleman, N.J. Coleman, Hydrothermal synthesis of zeolites from green container glass, Physicochem. Probl. Miner. Process. 56 (5) (2020) 784–796.

**[48]** Y. Kang, B. Swain, B. Im, J.-H. Yoon, K.H. Park, C.G. Lee, D.G. Kim, Synthesis of zeolite using aluminum dross and waste LCD glass powder: a waste to waste integration valorization process, Metals 9 (2019) 1240, https://doi.org/10.3390/ met9121240.

**[49]** A.R. Majdinasab, Q. Yuan, Microwave synthesis of zeolites from waste glass cullet using indirect fusion and direct hydrothermal methods: a comparative study, Ceram. Int 45 (2019) 2400–2410.

**[50]** A. Rozhkovskaya, J. Rajapakse, Graeme J. Millar, Process engineering approach to conversion of alum sludge and waste glass into zeolite LTA for water softening, J. Water Process. Eng. 43 (2021), 102177.

**[51]** R. Terzano, C. D'Alessandro, M. Spagnuolo, M. Romagnoli, L. Medici, Facile zeolite synthesis from municipal glass and aluminum solid wastes, Clean Soil Air Water 43 (1) (2015) 133–140.

**[52]** J. Alves, E.R.S. Dantas, S.B.C. Pergher, D.M. de, A. Melo, M.A.F. Melo, Synthesis of high value-added zeolitic materials using glass powder residue as a silica source, Mater. Res 17 (2014) 213–218.

**[53]** Z. Yao, D. Wu, J. Liu, W. Wu, H. Zhao, J. Tang, Recycling of typical difficult-to- treat e-waste: Synthesize zeolites from waste cathode-ray-tube funnel glass,

J. Hazard. Mater. 324 (2017) 673–680, https://doi.org/10.1016/j. jhazmat.2016.11.041.

**[54]** M. Tsujiguchi, T. Kobashi, M. Oki, Y. Utsumi, N. Kakimori, A. Nakahira, Synthesis and characterization of zeolite A from crushed particles of aluminoborosilicate glass used in LCD panels, J. Asian Ceram. Soc. 2 (2014) 27–32.

**[55]** A. Majdinasab, Q. Yuan, Microwave synthesis of zeolites from waste glass cullet using landfill leachate as a novel alternative solvent, Mater. Chem. Phys. 223 (2019) 613–622, https://doi.org/10.1016/j.matchemphys.2018.11.049.

**[56]** A.R. Majdinasab, Q. Yuan, Microwave synthesis of zeolites from waste glass cullet using indirect fusion and direct hydrothermal methods: a comparative study, Ceram. Int. (2018) 1–11, https://doi.org/10.1016/j.ceramint.2018.10.159.

**[57]** A.R. Majdinasab, P.K. Y, J. Wroczynskyj, N. Van Lierop, G.K. Cicek, Tranmer, Cost- effective zeolite synthesis from waste glass cullet using energy efficient microwave radiation, Mater. Chem. Phys. 221 (2019) 272–287, https://doi.org/10.1016/j. matchemphys.2018.09.057.

**[58]** X. Zeng, X. Hu, H. Song, G. Xia, Z.-Y. Shen, R. Yu, M. Moskovits, Microwave synthesis of zeolites and their related applications, Microporous Mesoporous Mater. 323 (2021), 111262.

**[59]** H.A. El Batal, M.Y. Hassan, M.A. Fanny, M.M. Ibrahim, Optical and FT infrared absorption spectra of soda lime silicate glasses containing nano Fe2O3 and effects of gamma irradiation, Silicon 9 (2017) 511–517.

**[60]** N.J. Coleman, Optical and FT infrared absorption spectra of soda lime silicate glasses containing nano Fe2O3 and effects of gamma irradiati, Int. J. Environ. Waste Manag. 8 (3/4) (2011) 366–382.

**[61]** S.S. Kouassi, J. Andji, J.P. Bonnet, S. Rossignol, Dissolution of waste glasses in high alkaline solutions, Ceram. Silik. 54 (3) (2010) 235–240.

14

**[62]** S.A. MacDonald, C.R. Schardt, D.J. Masiello, J.H. Simmons, Dispersion analysis of FTIR reflection measurements in silicate glasses, J. Non-Cryst. Solids 275 (2000) 72–82.

**[63]** I. Garcia Lodeiro, D.E. Macphee, A. Fernandez-Jimenez, Effect of alkalis on fresh CS-H gels. FTIR analysis, Cem. Concr. Res. 39 (2009) 147–153.

**[64]** C.I. Merzbacher, K.J. McGrath, P.L. Higby, 29Si NMR and infrared reflectance spectroscopy of low-silica calcium aluminosilicate glasses, J. Non Cryst. Solids 136 (1991) 249–259.

**[65]** Z. Jiang, J. Yang, H. Ma, L. Wang, X. Ma, Reaction behaviour of Al2O3 and SiO2 in high alumina coal fly ash during alkali hydrothermal process, Trans. Nonferr. Met. Soc. China 25 (2015) 2065–2072.

**[66]** W. Mozgawa, M. Kro´l, K. Barczyk, FT-IR studies of zeolites from different structural groups, Chemik 7 (65) (2011) 671–674.

**[67]** A.G. Stepanov, Basics of solid-state NMR for application in zeolite science: material and reaction characterization, in: B. Sels, L. Kustov (Eds.), Zeolites and Zeolite-like Materials Chapter 4, Elsevier, 2016.

**[68]** M. Thommes, K. Kaneko, A.V. Neimark, J.P. Olivier, F. Rodriguez-Reinoso, J. Rouquerol, et al., Physisorption of gases, with special reference to the evaluation of surface area and pore size distribution (IUPAC technical report), Pure Appl. Chem. 87 (9–10) (2015) 1051.

**[69]** K.S.W. Sing, R.T. Williams, Physisorption hysteresis loops and the characterization of nanoporous materials, Adsorpt. Sci. Technol. 22 (10) (2004) 773–782.

**[70]** L. Xu, J. Zhang, J. Ding, T. Liu, G. Shi, X.L. W, Y. Dang, R. Cheng, Guo, Pore structure and fractal characteristics of different shale lithofacies in the dalong formation in the western area of the lower yangtze platform, Minerals 10 (2020)

**[71]** L.Qiang, Z.Ying, C.Zhijun, G.Wei, C.Lishan, Influence of synthesis parameters on the crystallinity and Si/Al ratio of NaY zeolite synthesized from kaolin, Pet. Sci. 7 (2010) 403–409. Journal of Environmental Chemical Engineering 10 (2022) 108561

**[72]** M. Dietzel, Dissolution of silicates and the stability of polysilicic acid, Geochim. Cosmochim. Acta 64 (2000) 3275.